nanomaterials

MDPI

Article

$CrPS_4$ Nanoflakes as Stable Direct-Band-Gap 2D Materials for Ultrafast Pulse Laser Applications

Wenyao Zhang [1,†], Yu Zhang [1,†], Xudong Leng [2], Qun Jing [2] and Qiao Wen [1,*]

[1] Key Laboratory of Optoelectronic Devices and Systems of Ministry of Education and Guangdong Province, College of Physics and Optoelectronic Engineering, Shenzhen University, Shenzhen 518060, China
[2] Xinjiang Key for Laboratory of Solid State Physics and Devices, Xinjiang University, 777 Huarui Street, Urumqi 830017, China
* Correspondence: wenqiao@szu.edu.cn
† These authors contributed equally to this work.

Abstract: Two-dimensional (2D) materials have attracted considerable attention due to their potential for generating ultrafast pulsed lasers. Unfortunately, the poor stability of most layered 2D materials under air exposure leads to increased fabrication costs; this has limited their development for practical applications. In this paper, we describe the successful preparation of a novel, air-stable, and broadband saturable absorber (SA), the metal thiophosphate $CrPS_4$, using a simple and cost-effective liquid exfoliation method. The van der Waals crystal structure of $CrPS_4$ consists of chains of CrS_6 units interconnected by phosphorus. In this study, we calculated the electronic band structures of $CrPS_4$, revealing a direct band gap. The nonlinear saturable absorption properties, which were investigated using the P-scan technique at 1550 nm, revealed that $CrPS_4$-SA had a modulation depth of 12.2% and a saturation intensity of 463 MW/cm^2. Integration of the $CrPS_4$-SA into Yb-doped fiber and Er-doped fiber laser cavities led to mode-locking for the first time, resulting in the shortest pulse durations of 298 ps and 500 fs at 1 and 1.5 μm, respectively. These results indicate that $CrPS_4$ has great potential for broadband ultrafast photonic applications and could be developed into an excellent candidate for SA devices, providing new directions in the search for stable SA materials and for their design.

Keywords: metal thiophosphates; direct band gap; broadband; ultrafast photonic

check for updates

Citation: Zhang, W.; Zhang, Y.; Leng, X.; Jing, Q.; Wen, Q. $CrPS_4$ Nanoflakes as Stable Direct-Band-Gap 2D Materials for Ultrafast Pulse Laser Applications. *Nanomaterials* **2023**, *13*, 1128. https://doi.org/10.3390/nano13061128

Academic Editor: Filippo Giannazzo

Received: 27 February 2023
Revised: 17 March 2023
Accepted: 20 March 2023
Published: 22 March 2023

Copyright: © 2023 by the authors. Licensee MDPI, Basel, Switzerland. This article is an open access article distributed under the terms and conditions of the Creative Commons Attribution (CC BY) license (https://creativecommons.org/licenses/by/4.0/).

1. Introduction

Ultrafast laser pulses can be generated by converting a continuous laser wave into a short pulse train via a mode-locking method that has attracted considerable interest from various fields of science and technology, including material processing, the semiconductor industry, and advanced instrumentation [1–6]. A saturable absorber (SA) is a vital component of mode-locking technology. An SA generates ultrafast pulsed lasers through its nonlinear optical properties, which can periodically modulate the circulated light field in the laser cavity and thus satisfy the ever-growing demand for multiple technological applications [7–10]. As a result of the sustained efforts of scientists to discover SA materials with valuable properties, such as the semiconductor saturable-absorber mirror (SESAM) [11,12], many two-dimensional (2D) layered materials have now been considered as alternative systems [13–16]. 2D materials are characterized by their chemical diversity and structural complexity, as well as their unique optical and magnetic properties [17–19]. Moreover, semiconductor materials with direct band gaps have become important in a range of technologies such as solar cells and lasers. Their strong light absorption and ability to facilitate efficient light emission make them highly desirable for these applications [20–24]. As a result, several direct-band-gap semiconductors have been developed, including black phosphorus (BP) [25–27] and transition metal dichalcogenides (TMDs), for designing mode-locked fiber lasers [28] such as WSe_2 and MoS_2 [29,30]. BP has gained a great deal of

attention on account of its outstanding performance and inherent layer-dependent direct-band-gap energy. However, utilizing BP in practical applications remains a challenge due to its vulnerability to instability when exposed to ambient conditions [31–33]. In recent years, to improve the stability of BP, researchers have used various physical processing routes, such as surface passivation, O_2 plasma etching, ALD, transfer techniques, and self-assembly, to form different capping layers such as graphene, AlO_x, SiO_2, TiO_x, and polymers [34,35]. Scientists have also employed a variety of strategies to chemically protect BP materials, such as covalent functionalization (the formation of P–Ti, P=N, and P–O bonds) and elemental doping, as well as surface treatment [36–38]. However, the optimal means of protecting and passivating BP remains to be determined, and there is still an urgent need to discover novel and air-stable 2D materials for use as SAs.

Metal thiophosphates, such as $CrPS_4$, are 2D materials with excellent optical, electronic, and magnetic properties [39–44]. In the case of monolayer $CrPS_4$, the density-functional theory (DFT) describes it as a bipolar ferromagnetic semiconductor with a Curie temperature of 58 K. In other words, $CrPS_4$ is a candidate magnetic van der Waals (vdW) material [45]. Moreover, the peculiar in-plane anisotropy makes few-layer $CrPS_4$ flakes a birefringent material having monoclinic symmetry with space group *C*2 (No. 5), with two optical axes [46]. In addition, a lack of inversion symmetry in the crystal structure means that $CrPS_4$ may be used as a second-harmonic generation optical material. In short, $CrPS_4$ has attracted considerable interest in a number of fields due to its superior physical properties. However, to the best of our knowledge, the saturable absorption properties of $CrPS_4$ have yet to be fully studied. The potential of ultrafast photonic devices based on $CrPS_4$ flakes also remains unexplored. This prompted us to investigate whether $CrPS_4$ flakes could be a promising SA material. Furthermore, compared to other SAs with binary elements (WSe_2 and MoS_2), the incorporation of a third element in 2D ternary materials might introduce new degrees of freedom, potentially leading to more intriguing device applications.

In the study reported below, theoretical calculations show that $CrPS_4$ is a direct-band-gap semiconductor; that is, it can emit almost all energy in the form of light, indicating that it has potentially good saturable absorption properties, like monolayer MoS_2 and BP. It is also worth noting that, due to their multibonded crystal structure and chemical composition, $CrPS_4$ flakes exhibit remarkable stability even when exposed to air; in other words, the material could potentially be air-stable [47]. We then demonstrate the nonlinear optical absorption of $CrPS_4$ flakes prepared by the ultrasound-assisted liquid-phase exfoliation (LPE) method via the P-scan technique, and determine the modulation depth and the saturation intensity to be 12.2% and 463 MW/cm^2, respectively. Finally, by dripping few-layer $CrPS_4$ onto D-shaped fiber, a few-layer $CrPS_4$-SA is fabricated and applied for passively mode-locked YDFLs and EDFLs, with ultrashort pulse widths of 298 ps and 500 fs, respectively. By such means, we confirm that $CrPS_4$ has great potential in broadband ultrafast photonic applications. Our work provides a new paradigm for exploring the applications of metal thiophosphates in mode-locked fiber lasers.

2. Results and Discussion

Bulk $CrPS_4$ crystallized in the non-centrosymmetric monoclinic space group *C*2 (No. 5) at room temperature. The structure of layered $CrPS_4$ is shown in Figure 1a. The crystal structure was composed of distorted CrS_6 octahedra and PS_4 tetrahedra connected into a 2D double layer through chemical covalent bonds in a horizontal direction and vdWs forces along the *c* axis. The sheet thickness was 3.69 Å. Structurally, according to previous reports, the weak vdWs gap between layers was about 2.46 Å; this means that the few-layer form could be readily obtained from bulk samples by the LPE method. More importantly, the multibonded crystal structure of $CrPS_4$, in contrast to the lone-pair electrons found in BP, gave it the potential for air stability. It is commonly known that layered BP possesses a honeycomb structure in which a phosphorus atom is covalently bonded to three neighboring atoms through their *p*-orbitals, exposing a pair of lone-pair electrons (Figure 1b). The lone pairs of phosphorus atoms can readily react with oxygen to form P_xO_y; this ultimately

leads to the formation of phosphoric acid and H_2O, and thereby presents a significant obstacle to the use of BP in applications involving flexible electronics and photoelectronics.

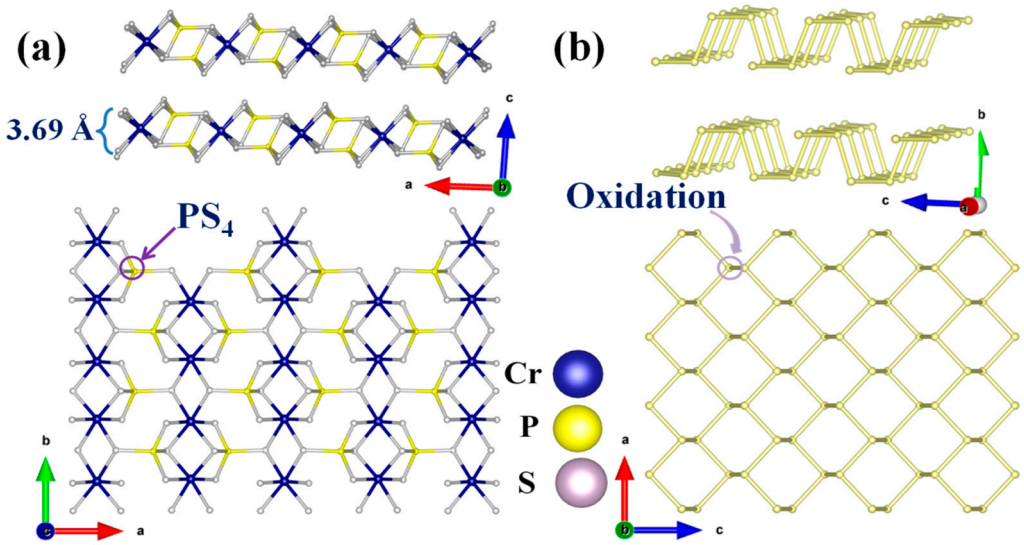

Figure 1. Schematic diagrams of crystal structures of layered (**a**) $CrPS_4$ and (**b**) BP. (The arrows represent the three coordinate axes of the crystallographic coordinate system.)

To gain deeper insights into the band-structure properties of $CrPS_4$, the CASTEP mode in Material Studio software was utilized to perform DFT calculations of the band structure and density of states (DOS) of both bulk and monolayer forms of $CrPS_4$ [48]. The calculated electronic band structures of bulk and monolayer $CrPS_4$ are illustrated in Figure 2b,c; these indicate that $CrPS_4$ is a direct-band-gap semiconductor, in agreement with previous research [49]. From Figure 2b, it can be seen that the bulk $CrPS_4$ nanoflakes exhibited a band-gap energy of 0.97 eV. As the number of layers decreased, the energy of the band gap increased. When the $CrPS_4$ nanoflakes were monolayered, the band-gap energy increased to about 2.15 eV. As illustrated in Figure 2d, the DOS plots reveal significant spin splitting in the d-orbitals of Cr atoms, indicating the presence of a sizable spin polarization in the bulk system.

Using the LPE method, few-layer $CrPS_4$ nanoflakes were exfoliated simply and effectively. Subsequently, we demonstrated the powder X-ray diffraction (XRD) patterns of $CrPS_4$ and its samples after exfoliation treatment by XRD spectroscopy, as illustrated in Figure 3a. It can be seen that the positions of the diffraction peaks on the two patterns were in almost perfect agreement with a standard PDF card of $CrPS_4$ (PDF #30-0411), indicating the integrity of the structure after exfoliated $CrPS_4$ nanoflakes were obtained. In addition, the diffraction pattern from the $CrPS_4$ sample was analyzed using X'pert Highscore Plus 3.0 [50]. The characterization of the diffraction pattern occurred in the range of 2θ = 10–70°, as shown in Figure S1. The diffraction pattern from the sample matched well with the diffraction pattern from the previous report. The reference code of $CrPS_4$ is 00-033-0404 [51]. The vibrational modes of the $CrPS_4$ were verified by the Raman spectrum and detected in the range 200–700 cm^{-1} (excitation wavelength: 532 nm, inVia, Renishaw, Wotton-under-Edge, UK) at room temperature. As shown in Figure 3b, about 13 vibration peaks were found in the Raman spectrum; this was in agreement with previously reported results [46], and further confirmed the rationality of the structure of the $CrPS_4$. The surface morphology of the samples as exfoliated was then analyzed via scanning electron microscope (SEM, JSM-5910LV, JEOL, Tokyo, Japan). As depicted in Figure 3c, the $CrPS_4$ nanoflakes exhibited an obvious layered structure, indicating that the nanoflakes were successfully fabricated based on the LPE method. The morphology of the $CrPS_4$ nanoflakes was also tested using an atomic force microscope (AFM, MFP-3D Infinity, Asylum Research, Oxford, UK), which can observe the lateral size of nanoflakes. Figure 3d,e show $CrPS_4$ nanoflakes with an average

thickness of ~25 nm. The linear optical transmission spectrum of exfoliated $CrPS_4$ was also detected using a UV-vis-NIR spectrophotometer (LAMBDA, Perkin Elmer Inc., Waltham, MA, USA). We found that, at wavelengths of 1030 and 1530 nm, the transmittances were approximately 91.7% and 93.3%, respectively (Figure 3f). BP has attracted tremendous interest because of its natural layer-dependent direct-band-gap energy, but layered BP is unstable and degrades rapidly in ambient conditions within hours. Calculated results indicated that $CrPS_4$ is also a direct-band-gap semiconductor, and this made us keen to discover if it was stable in ambient conditions for long time periods. Firstly, taken together, the powder XRD and Raman spectroscopy studies clearly demonstrated that the $CrPS_4$ structure remained stable after months in ambient conditions. As shown in Figure S1a, the intensity and peak position of $CrPS_4$, both as exfoliated and after ~2 months in air, remained essentially unchanged. The intensity and peak position of the Raman modes of $CrPS_4$ also remained essentially unchanged for ~2 months, indicating the air-stability of $CrPS_4$ (shown in Figure 3b). The $CrPS_4$ nanoflakes were then analyzed via energy-dispersive X-ray spectroscopy (EDS, Oxford Instruments, Oxford, UK). As depicted in Figure S1c,d, an average Cr/P/S molar ratio of 1.0:1.0:4.0 was recorded for $CrPS_4$ nanoflakes as exfoliated and again after ~2 months in air, further confirming the air-stability of the samples. To more intuitively demonstrate this stability after exposure to air for about 2 months, the surface morphology of the sample was analyzed via SEM. As can be seen in Figure S1c, the $CrPS_4$ nanoflakes continued to exhibit an obvious layered structure.

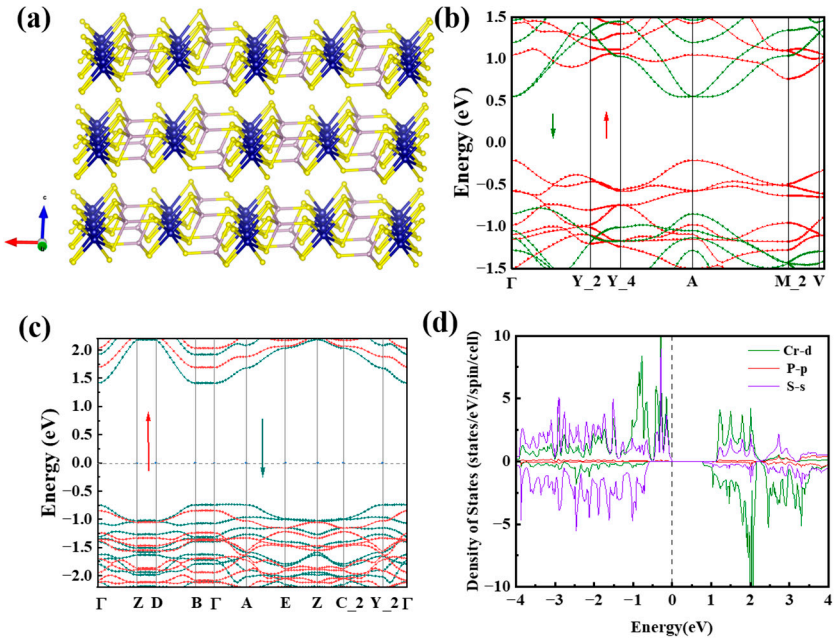

Figure 2. (**a**) Structure of $CrPS_4$ (The arrows represent the three coordinate axes of the crystallographic coordinate system); (**b**,**c**) electronic band structures of the bulk and monolayer $CrPS_4$ materials calculated by the HSE06 function (The red arrow denotes spin-up bands, while the green arrow represents spin-down bands in the energy band structure.); (**d**) DOS of the bulk $CrPS_4$.

The obtained few-layer $CrPS_4$ nanoflakes were then dripped onto the D-shaped fiber to form an SA device. To investigate the nonlinear optical properties of the $CrPS_4$-SA, a dual-channel balanced detection measurement system based on an erbium-doped fiber laser (1550 nm, 100 fs, 8.05 MHz) was employed, as shown in Figure 4 inset. Equation (1) only considers the case of single-photon absorption, and the nonlinear saturated absorption curve of $CrPS_4$-SA was obtained after fitting [52,53].

$$T(I) = 1 - \Delta T \times \exp\left(\frac{-I}{I_{sat}}\right) - T_{ns} \quad (1)$$

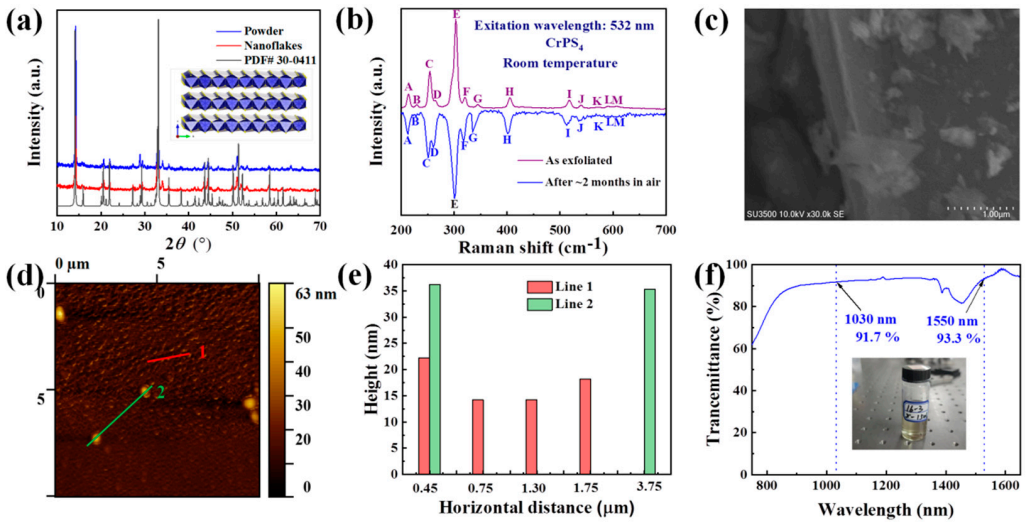

Figure 3. Characterizations of as-synthesized $CrPS_4$ nanoflakes after liquid-phase exfoliation: (**a**) the XRD patterns of $CrPS_4$; (**b**) the Raman spectrum of few-layer $CrPS_4$ nanoflakes on a Si substrate; (**c**) SEM image of $CrPS_4$; (**d**,**e**) AFM image of few-layer $CrPS_4$ nanoflakes on a Si substrate and corresponding height profile (The red line and the green line represent the positions of the measured material thickness in the sample); (**f**) UV/Vis/NIR absorption spectrum of few-layer $CrPS_4$ nanosheets in NMP.

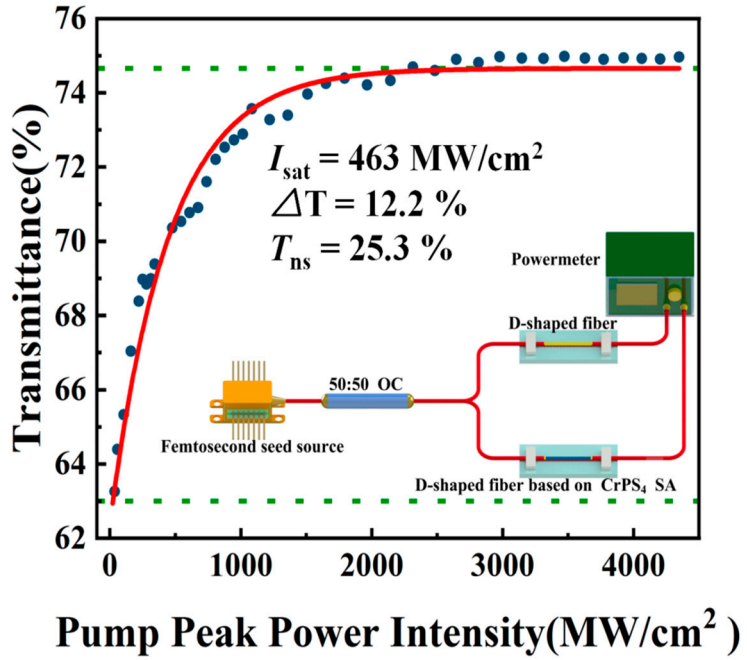

Figure 4. P-scan measurement system diagram and the corresponding nonlinear saturable absorption curve of $CrPS_4$.

In Equation (1), $T(I)$ is the transmission rate, ΔT is the modulation depth (MD), I is the input intensity, I_{sat} is the saturated intensity, and T_{ns} is the nonsaturable loss (NL). The fitting results are shown in Figure 4. Values of MD, I_{sat}, and NL were found to be ~12.2%, ~463 MW/cm^2, and ~25.3%, respectively.

Next, to validate the excellent potential of the layered $CrPS_4$ for ultrafast laser applications, we constructed 1.0 μm and 1.5 μm all-fiber laser cavities using Er-doped or Yb-doped fibers. The structural diagram of the optical fiber laser structure is shown in Figure 5. The laser cavity consisted of a section of Er-doped or Yb-doped fiber, a laser

diode (980 nm Pump Laser, Hanyu, Shanghai, China), a wavelength division multiplexer (WDM, Mingchuang, Shenzhen, China), an optical coupler (OC, Mingchuang, Shenzhen, China), a polarization-independent optical isolator (ISO, Mingchuang, Shenzhen, China), a polarization controller (PC, General Photonics, Losa Angeles, US), and a D-shaped fiber based on $CrPS_4$-SA. ISO and PC were used to ensure the unidirectional propagation of light and to adjust its polarization state, respectively. The evanescent field length of the D-shaped fiber optic bare leak was 10 mm, and the distance between the surface and the core was 1 μm. The Er-doped fiber laser cavity length was 21.96 m, including 4 m EDF (Nufern EDFC-980-HP, Hanyu, Shanghai, China) and 17.96 m single-mode fiber (SMF, Hanyu, Shanghai, China), with dispersion parameters at 1530 nm of −12.2 ps/(km·nm) and 18 ps/(km·nm), respectively. The net dispersion was estimated as −0.39 ps^2. Similarly, the cavity length of Yb-doped laser consisted of 1 m YDF (Nufern SM-YSF-HI-6/125, Hanyu, Shanghai, China) and 15.56 m single-mode fiber (HI1060), and the net dispersion of the cavity was estimated at 0.35 ps^2. The pulse performance of the laser output was determined by a power meter, a spectrum analyzer (AQ6370C, Yokogawa, Tokyo, Japan), a photodetector (DET08CFC/M 5 GHz, Thorlabs, Newton, MA, USA), a hybrid oscilloscope (DP04104B 1 GHz/s, Tektronix, OR, USA), and autocorrelator monitoring (PulseCheck, APE, Berlin, Germany). The temperature and humidity of the ultra-clean laboratory were 16.8 °C and 58%, respectively.

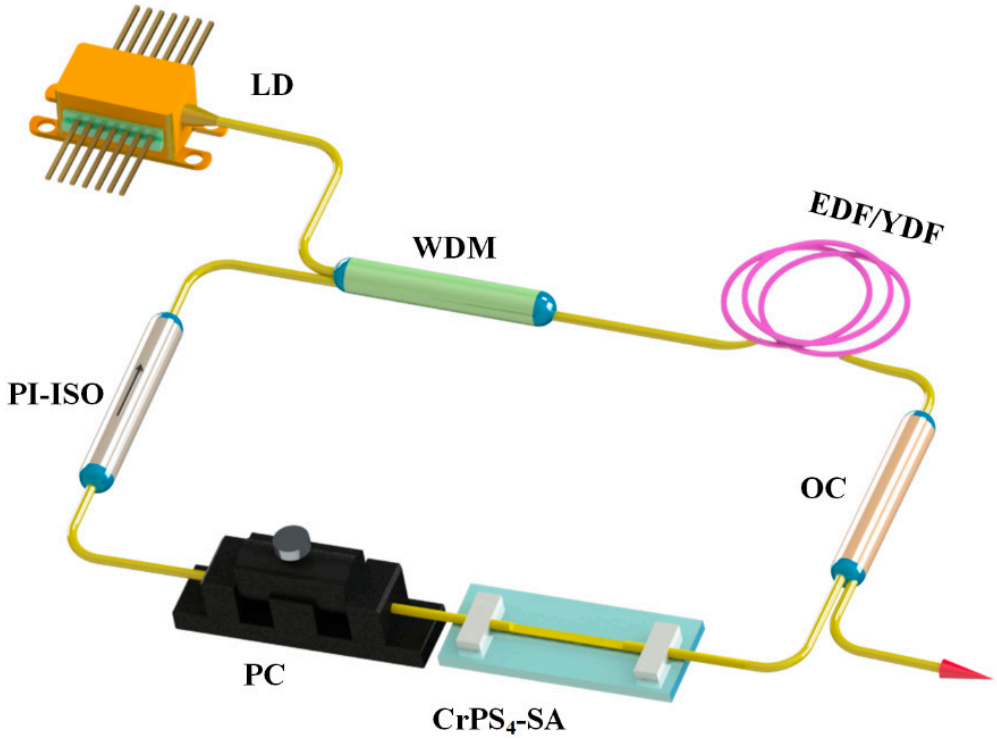

Figure 5. The cavity schematic for the fiber laser.

Importantly, we performed pre-experiments to demonstrate that, in the absence of SA, no mode-locking occurred in the laser cavity, regardless of PC modulation or pump power. By such means, we confirmed the authenticity of the experiment. After SA was applied to the laser cavity, we adjusted the PC while continuously increasing the pump power, and observed the output waveform of the oscilloscope. We achieved continuous-wave mode-locking (CWML) when the pump power was higher than 170 wm. When the pump power was increased to 300 mW, the output power was 10.64 mW, and pulse energy and peak power were 1.174 nJ and 3.94 W, respectively. The mode-locking sequence diagram is presented in Figure 6a, which shows a 110.4 ns time interval between adjacent pulses, which corresponds well to the pulse repetition rate of 9.05 MHz. The inset in Figure 6a

shows the amplitude intensity plot of the mode-locked pulse sequence; this indicates that the mode-locked sequence existed stably for a long time. The spectrum with a central wavelength of 1036.1 nm had a 3 dB spectral width of 0.84 nm, as shown in Figure 6b. The autocorrelation trace corresponding to the measured pulse at this time is shown in Figure 6c. It can be seen that the pulse width is about 298 ps, and the time-bandwidth product (TBP) is 69.9, indicating that the pulse has a serious chirp. In Figure 6d, a signal-to-noise ratio (SNR) measurement of approximately 55.3 dB can be observed with a higher signal peak at a laser cavity repetition rate of 9.05 MHz. The relationship between the mode-locked output power and pump power is shown in Figure 6e. When the pump power was 130 mW, the laser cavity output a continuous wave (CW). When the pump power was increased to 170 mW, the output was CWML, and the measured slope efficiency was about 4.9%. Subsequently, we measured the output spectrum of the laser cavity over a longer timescale, at time intervals of 1 h, for a total of 6 h. As shown in Figure 6f, the long-term spectrum was quite stable, indicating that a ytterbium-doped laser has the potential of highly stable operation.

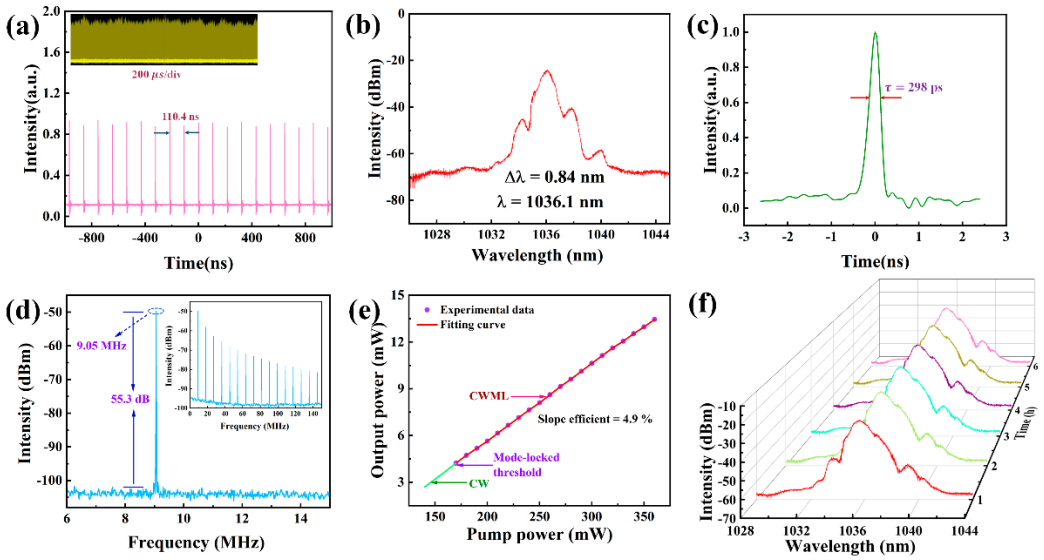

Figure 6. Classical mode-locked output characteristics: (**a**) pulse train; (**b**) optical spectrum; (**c**) pulse width; (**d**) RF spectrum (inset: broadband RF spectrum); (**e**) relative change of output power and pump power; (**f**) long-period spectroscopic measurement (1 h intervals, 6 h in total).

In order to verify that $CrPS_4$ could work in a wide wavelength range, we placed the additionally prepared $CrPS_4$-SA into an erbium-doped fiber laser cavity for debugging. Stable CWML output was achieved by adjusting the PC when the pump power was above 150 mW. The output power, pulse energy, and peak power were 6.1 mW, 0.893 nJ, and 1786 W, respectively, when the pump power was 270 mW. The output pulse characteristics are shown in Figure 7. The mode-locked pulse sequence is shown in Figure 7a. The pulse period was 146.4 ns, which corresponded to a pulse repetition rate of 6.83 MHz. The inset shows that the mode-locking was quite stable. Figure 7b shows the laser spectrum centered at 1531.6 nm with a 3 dB bandwidth of 5.6 nm. A measured pulse width of 500 fs resulted in a TBP of 0.35, as shown in Figure 7c. It can be clearly observed that the peak value of the high signal at the mode-locked repetition frequency was 6.83 MHz, and the signal-to-noise ratio was about 64 dB, as shown in Figure 7d. Figure 7e shows that the average output power varied linearly with increasing pump power, with a slope efficiency of 2.2%. Subsequently, we also measured the spectrum for 6 h, at time intervals of 1 h, and found that the erbium-doped laser mode-locking was very stable, as shown in Figure 7f.

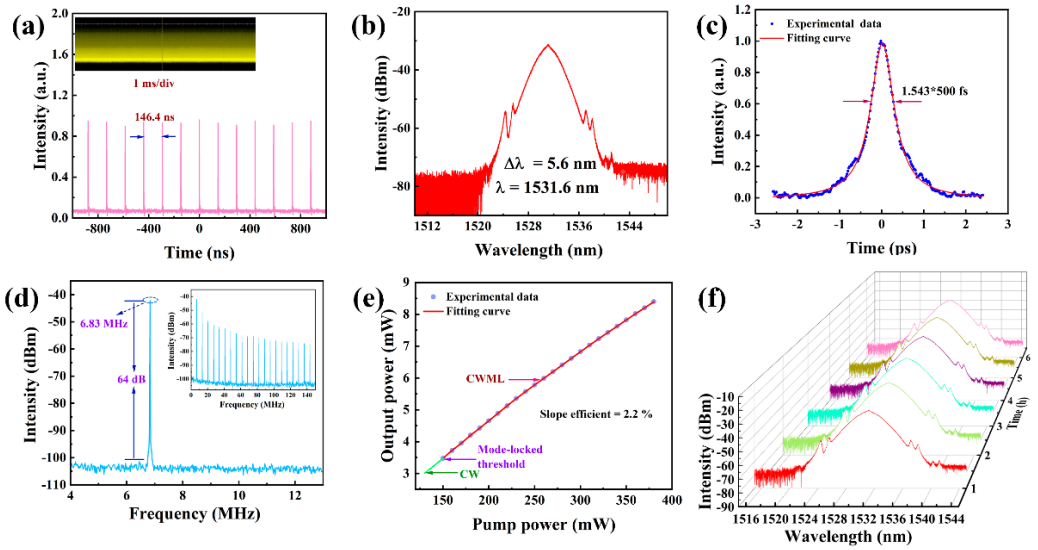

Figure 7. Classical mode-locked output characteristics: (**a**) pulse train; (**b**) optical spectrum; (**c**) pulse width; (**d**) RF spectrum (inset: broadband RF spectrum); (**e**) relative change of output power and pump power; (**f**) long-period spectroscopic measurement (1 h intervals, 6 h in total).

To demonstrate the stability of $CrPS_4$, we placed the previously prepared saturable absorber back into an ytterbium-doped fiber laser, 40 days after the first experiment, and found that the laser could still output mode-locked pulses after adjusting the pump and PC. The mode-locking output results are shown in Figure S3. The threshold of mode-locking was 180 mW, a slight increase (of 10 mW) compared to the first experiment. Figure S3a shows the pulse sequence with a pulse interval of 107.2 ns. The inset shows that the laser continued to work with high stability. Figure S3b shows that, in comparison with the first experiment, the central wavelength of the mode-locked spectrum remained the same, at 1036.1 nm, while the 3 dB bandwidth changed only slightly, from 0.84 nm to 0.8 nm. The measured mode-locking pulse width was 400 ps, as shown in Figure S3c, which was wider than the first measurement. The repetition frequency of the mode-locked strong signal peak was 9.32 MHz, and the SNR was about 52.6 dB, as shown in Figure S3d. The relationship between average output power and pump power is shown in Figure S3e, and the slope efficiency was 3.6%, which was slightly lower than the first time. We then measured the spectrum for 6 h, and the results are shown in Figure S3f. The spectrum remained unchanged, indicating that the laser worked stably, and that the $CrPS_4$ saturable absorber we made exhibited high stability.

Once again, 40 days after the first experiment, we put the previously used saturable absorber back into the erbium-doped fiber laser, using the adjustment method described above. To achieve CWML, pump power needed to be increased to more than 150 mw. The mode-locking output characteristics are shown in Figure S4. Figure S4a shows that the pulse interval was 136.9 ns, and the inset shows that the laser cavity remained in a stable state. Figure S4b shows that the central wavelength of the spectrum was 1531.4 nm, and the 3dB bandwidth was 6.2 nm, which was stable compared with the first experiment. Figure S4c shows that the mode-locked pulse width was 594 fs, which was slightly wider than the first experiment, with a TBP of 0.47. The signal-to-noise ratio of a strong signal peak at a repetition frequency of 7.33 MHz was approximately 69 dB. Figure S4e shows that the slope efficiency between the average output power and the pump power was 2.4%. Finally, we measured the long-term spectral changes, which indicated the excellent stability of the laser cavity, as shown in Figure S4f.

We then compared the data of the two experiments, as set out in Table 1. Although the two experiments were separated by 40 days, we found few differences in the results, indicating that the $CrPS_4$-SA we prepared had excellent stability. However, in order to more intuitively observe any variation in the experimental results, we drew a coefficient of

variation diagram to represent the degree of dispersion of the pulse parameters of the two experiments, as shown in Figure 8. It can be seen that the coefficients of variation of the pulse width, output power, pulse energy, and coefficients of variation of the Yb-doped fiber laser were close to 30%, while the coefficient of variation of the peak power was as high as 59%. For Er-doped fiber lasers, the coefficients of variation of its pulse parameters were all less than 20%; among these, the coefficients of variation of pulse energy, peak power and slope efficiency were all less than 10%. In short, the output variation of the erbium-doped fiber laser cavity was lower, and this finding is related to the performance of the laser cavity itself. The ytterbium-doped fiber laser cavity worked in the total positive dispersion region, while the erbium-doped laser cavity worked in the anomalous dispersion region, and the optical solitons formed through the balance of dispersion and nonlinear effects were more stable.

Table 1. Comparison of data before and after the two experiments.

Gain Fiber	Experimental Conditions (mW)/Days	Pulse Width	Output Power (mW)	Pulse Energy (nJ)	Peak Power (W)	Center WaveLength (nm)	Slope Efficiency (%)
Yb	300/1	298 ps	10.63	1.174	3.94	1036.1	4.9
	300/40	400 ps	8	0.876	2.144	1036.1	3.6
Er	270/1	500 fs	6.1	0.893	1786	1531.6	2.2
	270/40	594 fs	7.02	0.961	1617.8	1531.4	2.4

Note: The experimental conditions include the pump power in milliwatts and the time interval between the two experiments.

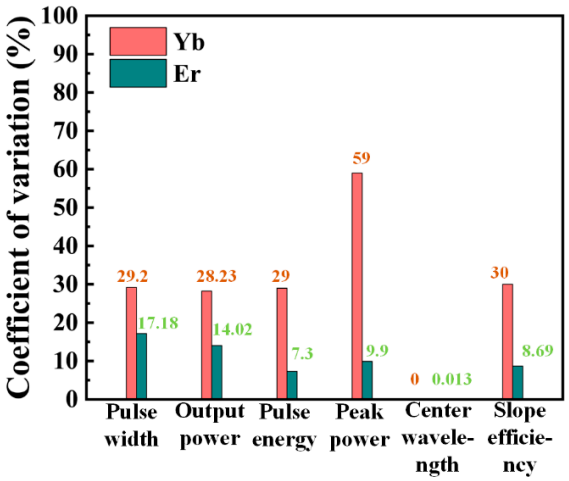

Figure 8. Diagram of the degree of dispersion of the output pulse parameters of the two experiments.

The pulse performance of the laser has a crucial influence on the application. In Table S1, we summarize the performance of mode-locked ytterbium-doped lasers for several representative 2D materials. It can be seen that the output of these ytterbium-doped lasers was in the order of picoseconds. In contrast, the output of our $CrPS_4$ ytterbium-doped fiber laser was 298 ps. These results show that $CrPS_4$ has higher generation efficiency for ultra-short pulse output, and has certain advantages in terms of pulse width. The maximum output power of our laser was 10.63 mW, which is 28.7 times that of the graphene previously reported by Zhao et al. [54], and 1.38 times that of the Mo_2C previously reported by Liu et al. [55]. The single-pulse energy of most YDF lasers using 2D materials as SA is usually limited to below 1 nJ; however, our laser achieved an output of 1.174 nJ, with a peak power of 3.94 W, which is 5.5 times that of the WS_2 reported by Mao et al. [56], and 2.3 times that of the $NiPS_3$ reported by Liu et al. [56]. In a similar way, we compared erbium-doped fiber lasers based on other 2D slave materials, as shown in Table S2. As can be readily

observed, because of the remarkable nonlinear optical properties of these 2D materials, their modulation depths vary in percentage terms from low single digits to many tens. In contrast, the modulation depth of our prepared $CrPS_4$ was 12.2%, which is higher than the 10.9% for BP reported by Chao et al. [57] and the 5.1% for Mo_2C reported by Liu et al. [55]. At the same time, our pulse output was 500 fs, which is similar to that achieved by other lasers. In addition, our output reached a level of 6.1 mW, which is twice that of the graphene reported by Bao et al. [7], and 2.3 times that of the BP reported by Chao et al. [57]. The single pulse energy and peak power were 893 pJ and 1786 W, respectively. Not only did we measure the stability of the spectrum over 6 h, we also re-experimented with the previously fabricated saturable absorber 40 days later and found that it still achieved mode locking. These experimental results confirm that $CrPS_4$ is a competitive direct-band-gap material with excellent nonlinear optical modulation properties and great potential for broadband ultrafast photonics applications.

3. Conclusions

In conclusion, we fabricated high-quality $CrPS_4$-SA by the LPE method. Theoretical calculations of the electronic band structures of $CrPS_4$ revealed a direct band gap. We studied the applications of few-layer $CrPS_4$-SA in ultrafast photonics for the first time. The saturated intensity and modulation depth of $CrPS_4$-SA were 463 MW/cm^2 and 12.2%, respectively, at 1.5 μm. Moreover, based on the excellent saturable absorption of the D-shaped $CrPS_4$ SA, the pulse characteristics of fiber lasers operating in conventional soliton states were measured. We successfully obtained picosecond mode-locked pulses of 298 ps and ultrashort femtosecond pulses of 500 fs in the 1 μm and 1.5 μm regions, respectively. The signal-to-noise ratio (SNR) of the mode-locked operation was as high as 55.3 dB at 9.05 MHz (YDFL), and 64 dB at 6.83 MHz (EDFL). More importantly, the few-layer $CrPS_4$ exhibited excellent stability during exposure to air for a period of time. Our experimental results show that $CrPS_4$ is an air-stable and broadband SA, with promising potential for ultrafast laser applications.

4. Experimental Section

Fabrication of $CrPS_4$. An LPE method was used to exfoliate few-layer $CrPS_4$ nanoflakes, in which the vdWs forced between the layers of $CrPS_4$ were broken by an ultrasonic wave. Firstly, commercially available high-purity $CrPS_4$ (Shenzhen six carbon) powder (about 23 mg) was ground in a mortar and dispersed into *N*-methyl-2-pyrrolidone (NMP, 30 mL), which was exfoliated in an ultrasonic cell disruptor for 20 h at power of 400 W. In order to make the solute to form nanoscale flakes, the solvent was ultrasonicated in an ultrasound cleaner for 24 h. Then, the mixture was centrifugally treated at a speed of 5000 rpm for 20 min to separate precipitation, and the few-layer $CrPS_4$ containing supernatant was obtained. All experimental procedures were conducted at room temperature (16.8 °C) and a relative humidity of 58%.

Characterization. The powder X-ray diffraction (XRD) patterns of $CrPS_4$ and its samples after exfoliated treatment were further demonstrated by XRD spectroscopy; the vibrational modes of the $CrPS_4$ were verified by Raman spectrum, and detected in the range 200–700 cm^{-1} (excitation wavelength: 532 nm, inVia, Renishaw, Wotton-under-Edge, UK) at room temperature. The surface morphology of the samples as exfoliated was analyzed via a scanning electron microscope. The morphology of $CrPS_4$ nanoflakes was also tested using an atomic force microscope and the linear optical transmission spectrum of exfoliated $CrPS_4$ was detected by an UV-vis-NIR spectrophotometer.

DFT calculation details. Here, the Vienna Ab initio Simulation Package (VASP, University of Vienna) was utilized to optimize the crystal structures and calculate electronic structures [58–60]. The exchange and correlative potentials of electron−electron interactions were accounted for using the generalized gradient approximation (GGA) within the Perdew−Burke−Eruzerhof (PBE) scheme [61,62]. More specifically, an energy cut-

off of 500 eV and a Monkhorst–Pack Brillouin zone sampling grid [63] with a resolution $0.02 \times 2\pi$ Å^{-1} were applied.

Supplementary Materials: The following supporting information can be downloaded at: https://www.mdpi.com/article/10.3390/nano13061128/s1: Figure S1: The diffraction pattern from $CrPS_4$ sample was analyzed using X'pert Highscore Plus 3.0; Figure S2: XRD spectra, SEM image, EDX spectra with an atomic ratio of Cr, P, and S elements for $CrPS_4$ flakes as exfoliated and after ~2 months in air; Figure S3: the results of typical mode-locked pulse characteristics (second experiment) at 1 μm after ~40 days; Figure S4: the results of typical mode-locked pulse characteristics(second experiment) at 1.5 μm after ~40 days; Table S1: comparison of SA with other 2D materials at 1 μm laser output parameters; Table S2: comparison of SA with other 2D materials at 1.5 μm laser output parameters. References [64–75] are cited in the supplementary materials.

Author Contributions: Conceptualization, Q.W.; methodology, W.Z.; software, Y.Z. and Q.W.; validation, Y.Z., W.Z., and X.L.; formal analysis, W.Z. and Q.J.; investigation, W.Z. and Y.Z.; resources, Y.Z.; data curation, W.Z.; writing—original draft preparation, W.Z. and Y.Z.; writing—review and editing, W.Z. and Y.Z.; visualization, W.Z. and Y.Z.; supervision, Q.W. and Q.J.; project administration, Q.W.; funding acquisition, Q.W. All authors have read and agreed to the published version of the manuscript.

Funding: This work was financially supported by the National Natural Science Foundation of China (6217030813), the Guangdong Basic and Applied Basic Research Foundation (2021A1515010964), and the Science and Technology Innovation Commission of Shenzhen Municipality (SGDX20190919094803949 and JCYJ20200109105810074).

Data Availability Statement: The data presented in this study are available on request from the corresponding author.

Conflicts of Interest: The authors declare no competing financial interest.

References

1. Zhang, Y.; Zhu, J.Q.; Li, P.X.; Wang, X.X.; Yu, H.; Xiao, K.; Li, C.Y.; Zhang, G.Y. All-fiber Yb-doped fiber laser passively mode-locking by monolayer MoS_2 saturable absorber. *Opt. Commun.* **2018**, *413*, 236–241. [CrossRef]
2. Sugioka, K.; Cheng, Y. Ultrafast lasers—Reliable tools for advanced materials processing. *Light Sci. Appl.* **2014**, *3*, e149. [CrossRef]
3. Keller, U. Recent developments in compact ultrafast lasers. *Nature* **2003**, *424*, 831–838. [CrossRef]
4. Gu, T.; Petrone, N.; McMillan, J.F.; van der Zande, A.; Yu, M.; Lo, G.Q.; Kwong, D.L.; Hone, J.; Wong, C.W. Regenerative oscillation and four-wave mixing in graphene optoelectronics. *Nat. Photonics* **2012**, *6*, 554–559. [CrossRef]
5. Fermann, M.E.; Hartl, I. Ultrafast fibre lasers. *Nat. Photonics* **2013**, *7*, 868–874. [CrossRef]
6. Du, Y.; Zhao, K.; Zhu, Z.L.; Wang, J.; Deng, W.J.; Liang, X.D. Research and application of ultrafast laser precision manufacturing technology. *Laser Infrared* **2020**, *50*, 1419–1425. [CrossRef]
7. Bao, Q.L.; Zhang, H.; Wang, Y.; Ni, Z.H.; Yan, Y.L.; Shen, Z.X.; Loh, K.P.; Tang, D.Y. Atomic-layer graphene as a saturable absorber for ultrafast pulsed lasers. *Adv. Funct. Mater.* **2009**, *19*, 3077–3083. [CrossRef]
8. Dong, Y.C.; Chertopalov, S.; Maleski, K.; Anasori, B.; Hu, L.Y.; Bhattacharya, S.; Rao, A.M.; Gogotsi, Y.; Mochalin, V.N.; Podila, R. Saturable absorption in 2D Ti_3C_2 MXene thin films for passive photonic diodes. *Adv. Mater.* **2018**, *30*, 1705714. [CrossRef]
9. Liu, S.X.; Huang, H.F.; Lu, J.S.; Xu, N.; Qu, J.L.; Wen, Q. Liquid-phase exfoliation of Ta_2NiS_5 and Its application in near-infrared mode-locked fiber lasers with evanescent field interactions and passively Q-switched bulk laser. *Nanomaterials* **2022**, *12*, 695. [CrossRef]
10. Zhang, A.J.; Wang, Z.H.; Ou-Yang, H.; Lyu, W.H.; Sun, J.X.; Cheng, Y.; Fu, B. Recent progress of two-dimensional materials for ultrafast photonics. *Nanomaterials* **2021**, *11*, 1778. [CrossRef]
11. Chen, L.L.; Zhang, M.; Zhou, C.; Cai, Y.; Ren, L.; Zhang, Z.G. Ultra-Low Repetition Rate SESAM-mode-locked Linear-cavity Erbium-doped Fiber Laser. In Proceedings of the 2009 Conference on Lasers & Electro Optics & The Pacific Rim Conference on Lasers and Electro-Optics, Shanghai, China, 20 August–3 September 2009; pp. 587–588.
12. Cabasse, A.; Ortac, B.; Martel, G.; Hideur, A.; Limpere, J. Highly normal dispersion Er-doped fiber laser mode-locked with a SESAM. In Proceedings of the 2008 Conference on Lasers and Electro-Optics and 2008 Conference on Quantum Electronics and Laser Science, San Jose, CA, USA, 4–9 May 2008; pp. 1–2.
13. Li, P.F.; Chen, Y.; Yang, T.S.; Wang, Z.Y.; Lin, H.; Xu, Y.H.; Li, L.; Mu, H.R.; Shivananju, B.N.; Zhang, Y.P.; et al. Two-dimensional $CH_3NH_3PbI_3$ perovskite nanosheets for ultrafast pulsed fiber lasers. *ACS Appl. Mater. Interfaces* **2017**, *9*, 12759–12765. [CrossRef]
14. Guo, B.; Xiao, Q.L.; Wang, S.H.; Zhang, H. 2D layered materials: Synthesis, nonlinear optical properties, and device applications. *Laser Photonics Rev.* **2019**, *13*, 1800327. [CrossRef]

15. Guo, X.; Wang, S.; Yan, P.G.; Wang, J.Z.; Yu, L.P.; Liu, W.J.; Zheng, Z.J.; Guo, C.Y.; Ruan, S.C. High modulation depth enabled by $Mo_2Ti_2C_3Tx$ MXene for Q-switched pulse generation in a mid-infrared fiber laser. *Nanomaterials* **2022**, *12*, 1343. [CrossRef]
16. Zhou, L.L.; Fu, H.G.; Lv, T.; Wang, C.B.; Gao, H.; Li, D.Q.; Deng, L.M.; Xiong, W. Nonlinear optical characterization of 2D materials. *Nanomaterials* **2020**, *10*, 2263. [CrossRef]
17. Jia, L.; Lei, T.M. Research progress on physical properties and chemical stability of two-dimensional black phosphorus. *Mater. Rev.* **2018**, *32*, 1100–1106. [CrossRef]
18. He, J.S.; Tao, L.L.; Zhang, H.; Zhou, B.; Li, J.B. Emerging 2D materials beyond graphene for ultrashort pulse generation in fiber lasers. *Nanoscale* **2019**, *11*, 2577–2593. [CrossRef]
19. Bundulis, A.; Alnis, J.; Shuklov, I.A.; Kim, V.V.; Lizunova, A.A.; Mardini, A.A.; Grube, J.; Razumov, V.F.; Ganeev, R.A. Nonlinear absorption and refraction of picosecond and femtosecond pulses in HgTe quantum dot films. *Nanomaterials* **2021**, *11*, 3351. [CrossRef]
20. Shah, A.; Torres, P.; Tscharner, R.; Wyrsch, N.; Keppner, H. Photovoltaic technology: The case for thin-film solar cells. *Science* **1999**, *285*, 692–698. [CrossRef]
21. Guo, Q.J.; Ford, G.M.; Yang, W.-C.; Walker, B.C.; Stach, E.A.; Hillhouse, H.W.; Agrawal, R. Fabrication of 7.2% efficient CZTSSe solar cells using CZTS nanocrystals. *J. Am. Chem. Soc.* **2010**, *132*, 17384–17386. [CrossRef]
22. Watanabe, K.; Taniguchi, T.; Kanda, H. Direct-bandgap properties and evidence for ultraviolet lasing of hexagonal boron nitride single crystal. *Nat. Mater.* **2004**, *3*, 404–409. [CrossRef]
23. Hochbaum, A.I.; Yang, P. Semiconductor nanowires for energy conversion. *Chem. Rev.* **2010**, *110*, 527–546. [CrossRef]
24. Bhaskar, S.; Visweswar Kambhampati, N.S.; Ganesh, K.M.; Srinivasan, V.; Ramamurthy, S.S. Metal-free, graphene oxide-based tunable soliton and plasmon engineering for biosensing applications. *ACS Appl. Mater. Interfaces* **2021**, *13*, 17046–17061. [CrossRef] [PubMed]
25. Sun, M.K.; Wang, Y.; Hu, H.; Zhang, H.; Li, W.J.; Lv, B.; Zhu, Z.; Guan, C.Y.; Shi, J.H. Optical properties and dynamic extrinsic chirality of structured monolayer black phosphorus. *Front. Mater.* **2022**, *9*, 826795. [CrossRef]
26. Zhang, M.; Wu, Q.; Zhang, F.; Chen, L.L.; Jin, X.X.; Hu, Y.W.; Zheng, Z.; Zhang, H. 2D black phosphorus saturable absorbers for ultrafast photonics. *Adv. Opt. Mater.* **2019**, *7*, 1800224. [CrossRef]
27. Li, L.; Wang, Y.G.; Wang, X. Ultrafast pulse generation with black phosphorus solution saturable absorber. *Laser Phys.* **2017**, *27*, 085104. [CrossRef]
28. Liu, X.; Gao, Q.; Zheng, Y.; Mao, D.; Zhao, J.L. Recent progress of pulsed fiber lasers based on transition-metal dichalcogenides and black phosphorus saturable absorbers. *Nanophotonics* **2020**, *9*, 2215–2231. [CrossRef]
29. Wang, J.T.; Chen, H.; Jiang, Z.K.; Yin, J.D.; Wang, J.Z.; Zhang, M.; He, T.C.; Li, J.Z.; Yan, P.G.; Ruan, S.C. Mode-locked thulium-doped fiber laser with chemical vapor deposited molybdenum ditelluride. *Opt. Lett.* **2018**, *43*, 1998–2001. [CrossRef]
30. Wang, J.L.; Wang, X.L.; Lei, J.J.; Ma, M.Y.; Wang, C.; Ge, Y.Q.; Wei, Z.Y. Recent advances in mode-locked fiber lasers based on two-dimensional materials. *Nanophotonics* **2020**, *9*, 2315–2340. [CrossRef]
31. Zhao, Y.T.; Wang, H.Y.; Huang, H.; Xiao, Q.L.; Xu, Y.H.; Guo, Z.; Xie, H.H.; Shao, J.D.; Sun, Z.B.; Han, W.J.; et al. Surface coordination of black phosphorus for robust air and water stability. *Angew. Chem. Int. Ed.* **2016**, *55*, 5003–5007. [CrossRef]
32. Wood, J.D.; Wells, S.A.; Jariwala, D.; Chen, K.-S.; Cho, E.; Sangwan, V.K.; Liu, X.L.; Lauhon, L.J.; Marks, T.J.; Hersam, M.C. Effective passivation of exfoliated black phosphorus transistors against ambient degradation. *Nano Lett.* **2014**, *14*, 6964–6970. [CrossRef]
33. Ziletti, A.; Carvalho, A.; Campbell, D.K.; Coker, D.F.; Castro Neto, A.H. Oxygen defects in phosphorene. *Phys. Rev. Lett.* **2015**, *114*, 046801. [CrossRef]
34. Zhao, Y.K.; Sun, Z.J.; Zhang, B.W.; Yan, Q.F. Unveiling the degradation chemistry of fibrous red phosphorus under ambient conditions. *ACS Appl. Mater. Interfaces* **2022**, *14*, 9925–9932. [CrossRef] [PubMed]
35. Tan, S.J.R.; Abdelwahab, I.; Chu, L.Q.; Poh, S.M.; Liu, Y.P.; Lu, J.; Chen, W.; Loh, K.P. Quasi-monolayer black phosphorus with high mobility and air stability. *Adv. Mater.* **2018**, *30*, 1704619. [CrossRef] [PubMed]
36. Luo, W.; Zemlyanov, D.Y.; Milligan, C.A.; Du, Y.C.; Yang, L.M.; Wu, Y.Q.; Ye, P.D. Surface chemistry of black phosphorus under a controlled oxidative environment. *Nanotechnology* **2016**, *27*, 434002. [CrossRef] [PubMed]
37. Song, H.Z.; Wu, H.; Ren, T.Q.; Yan, S.C.; Chen, T.H.; Shi, Y. Developments in stability and passivation strategies for black phosphorus. *Nano Res.* **2021**, *14*, 4386–4397. [CrossRef]
38. Pei, J.J.; Gai, X.; Yang, J.; Wang, X.B.; Yu, Z.F.; Choi, D.-Y.; Luther-Davies, B.; Lu, Y.R. Producing air-stable monolayers of phosphorene and their defect engineering. *Nat. Commun.* **2016**, *7*, 10450. [CrossRef]
39. Neal, S.N.; O'Neal, K.R.; Haglund, A.V.; Mandrus, D.G.; Bechtel, H.A.; Carr, G.L.; Haule, K.; Vanderbilt, D.; Kim, H.-S.; Musfeldt, J.L. Exploring few and single layer $CrPS_4$ with near-field infrared spectroscopy. *2D Mater.* **2021**, *8*, 035020. [CrossRef]
40. Synnatschke, K.; Shao, S.Q.; van Dinter, J.; Hofstetter, Y.J.; Kelly, D.J.; Grieger, S.; Haigh, S.J.; Vaynzof, Y.; Bensch, W.; Backes, C. Liquid exfoliation of $Ni_2P_2S_6$: Structural characterization, size-dependent properties, and degradation. *Chem. Mater.* **2019**, *31*, 9127–9139. [CrossRef]
41. Sibley, S.P.; Francisa, A.H.; Lifshitzb, E.; Clkmen, R. Magnetic resonance studies of intercalated, twodimensional transition metal chalcogenophosphate. *Colloids Surf. A Physicochem. Eng. Asp.* **1994**, *82*, 205–215. [CrossRef]
42. Budniak, A.K.; Killilea, N.A.; Zelewski, S.J.; Sytnyk, M.; Kauffmann, Y.; Amouyal, Y.; Kudrawiec, R.; Heiss, W.; Lifshitz, E. Exfoliated $CrPS_4$ with promising photoconductivity. *Small* **2020**, *16*, 1905924. [CrossRef]

43. Calder, S.; Haglund, A.V.; Liu, Y.; Pajerowski, D.M.; Cao, H.B.; Williams, T.J.; Garlea, V.O.; Mandrus, D. Magnetic structure and exchange interactions in the layered semiconductor $CrPS_4$. *Phys. Rev. B* **2020**, *102*, 024408. [CrossRef]
44. Kim, S.; Lee, J.; Jin, G.; Jo, M.-H.; Lee, C.G.; Ryu, S.M. Crossover between photochemical and photothermal oxidations of atomically thin magnetic semiconductor $CrPS_4$. *Nano Lett.* **2019**, *19*, 4043–4051. [CrossRef]
45. Peng, Y.X.; Ding, S.L.; Cheng, M.; Hu, Q.F.; Yang, J.; Wang, F.G.; Xue, M.Z.; Liu, Z.; Lin, Z.C.; Avdeev, M.; et al. Magnetic structure and metamagnetic transitions in the van der Waals antiferromagnet $CrPS_4$. *Adv. Mater.* **2020**, *32*, 2001200. [CrossRef]
46. Lee, J.; Ko, T.Y.; Kim, J.H.; Bark, H.; Kang, B.; Jung, S.-G.; Park, T.; Lee, Z.; Ryu, S.; Lee, C. Structural and optical properties of single- and few-layer magnetic semiconductor $CrPS_4$. *ACS Nano* **2017**, *11*, 10935–10944. [CrossRef]
47. Son, J.; Son, S.; Park, P.; Kim, M.; Tao, Z.; Oh, J.; Lee, T.; Lee, S.; Kim, J.; Zhang, K.X.; et al. Air-stable and layer-dependent ferromagnetism in atomically thin van der Waals $CrPS_4$. *ACS Nano* **2021**, *15*, 16904–16912. [CrossRef] [PubMed]
48. Momma, K.; Izumi, F. VESTA 3 for three-dimensional visualization of crystal, volumetric and morphology data. *J. Appl. Crystallogr.* **2011**, *44*, 1272–1276. [CrossRef]
49. Deng, J.; Guo, J.; Hosono, H.; Ying, T.; Chen, X. Two-dimensional bipolar ferromagnetic semiconductors from layered antiferromagnets. *Phys. Rev. Mater.* **2021**, *5*, 034005. [CrossRef]
50. Degen, T.; Sadki, M.; Bron, E.; König, U.; Nénert, G. *HighScore Suite*; Cambridge University Press: Cambridge, UK, 2014; Volume 29, pp. S13–S18.
51. Diehl, R.; Carpentier, C.-D. The crystal structure of chromium thiophosphate, $CrPS_4$. *Acta Crystallogr. Sect. B Struct. Sci. Cryst. Eng. Mater.* **1977**, *B33*, 1399–1404. [CrossRef]
52. Andrianov, A.; Kim, A.; Muraviov, S.; Sysoliatin, A. Wavelength-tunable few-cycle optical pulses directly from an all-fiber Er-doped laser setup. *Opt. Lett.* **2009**, *34*, 3193–3195. [CrossRef]
53. Chi, C.; Lee, J.; Koo, J.; Han Lee, J. All-normal-dispersion dissipative-soliton fiber laser at 1.06 μm using a bulk-structured Bi_2Te_3 topological insulator-deposited side-polished fiber. *Laser Phys.* **2014**, *24*, 105106. [CrossRef]
54. Zhao, L.M.; Tang, D.Y.; Zhang, H.; Wu, X.; Bao, Q.L.; Loh, K.P. Dissipative soliton operation of an ytterbium-doped fiber laser mode locked with atomic multilayer graphene. *Opt. Lett.* **2010**, *35*, 3622–3624. [CrossRef]
55. Liu, S.X.; Lu, J.S.; Huang, H.F.; Xu, N.; Qu, J.L.; Wen, Q. Ultrafast photonics applications based on evanescent field interactions with 2D molybdenum carbide (Mo_2C). *J. Mater. Chem. C* **2021**, *9*, 6187–6192. [CrossRef]
56. Mao, D.; Zhang, S.L.; Wang, Y.D.; Gan, X.T.; Zhang, W.D.; Mei, T.; Wang, Y.G.; Wang, Y.S.; Zeng, H.B.; Zhao, J.L. WS_2 saturable absorber for dissipative soliton mode locking at 1.06 and 1.55 microm. *Opt. Express* **2015**, *23*, 27509–27519. [CrossRef] [PubMed]
57. Chao, L.Z.; Meng, L.; Nan, G.Z.; Fang, J.X.; Ping, L.A.; Jun, Z.H.; Feng, Y.X.; Cheng, X.W.; Han, Z. Microfiber-based few-layer black phosphorus saturable absorber for ultra-fast fiber laser. *Opt. Express* **2015**, *23*, 20030–20039. [CrossRef]
58. Kresse, G.; Hafner, J. Norm-conserving and ultrasoft pseudopotentials for first-row and transition elements. *J. Phys. Condens. Matter* **1994**, *6*, 8245–8257. [CrossRef]
59. Kresse, G.; Furthmüller, J. Efficiency of ab-initio total energy calculations for metals and semiconductors using a plane-wave basis set. *Comput. Mater. Sci.* **1996**, *6*, 15–50. [CrossRef]
60. Kresse, G.; Furthmüller, J. Efficient iterative schemes for ab initio total-energy calculations using a plane-wave basis set. *Phys. Rev. B Cover. Condens. Matter Mater. Phys.* **1996**, *54*, 11169–11186. [CrossRef]
61. Bader, R.F.W. A quantum theory of molecular structure and its applications. *Chem. Rev.* **1991**, *91*, 893–928. [CrossRef]
62. Perdew, J.P.; Burke, K.; Ernzerhof, M. Generalized gradient approximation made simple. *Phys. Rev. Lett.* **1996**, *77*, 3865–3868. [CrossRef] [PubMed]
63. Monkhorst, H.J.; Pack, J.D. Special points for Brillouin-zone integrations. *Phys. Rev. B* **1976**, *13*, 5188–5192. [CrossRef]
64. Huang, S.S.; Wang, Y.G.; Guang, Y.P.; Zhang, G.L.; Zhao, J.Q.; Li, H.Q.; Lin, R.Y.; Cao, G.Z.; Duan, J.A. Observation of multipulse bunches in a graphene oxide passively mode-locked ytterbium-doped fiber laser with all-normal dispersion. *Appl. Phys. B* **2014**, *116*, 939–946. [CrossRef]
65. Al-Masoodi, A.H.H.; Yasin, M.; Ahmed, M.H.M.; Latiff, A.A.; Arof, H.; Harun, S.W. Mode-locked ytterbium-doped fiber laser using mechanically exfoliated black phosphorus as saturable absorber. *Optik* **2017**, *147*, 52–58. [CrossRef]
66. Song, H.; Wang, Q.; Zhang, Y.; Li, L. Mode-locked ytterbium-doped all-fiber lasers based on few-layer black phosphorus saturable absorbers. *Opt. Commun.* **2017**, *394*, 157–160. [CrossRef]
67. Jiang, X.T.; Liu, S.X.; Liang, W.Y.; Luo, S.j.; He, Z.L.; Ge, Y.Q.; Wang, H.D.; Cao, R.; Zhang, F.; Wen, Q.; et al. Broadband nonlinear photonics in few-layer MXene $Ti_3C_2T_x$ (T = F, O, or OH). *Laser Photonics Rev.* **2018**, *12*. [CrossRef]
68. Samikannu, S.; Sivaraj, S. Dissipative soliton generation in an all-normal dispersion ytterbium-doped fiber laser using few-layer molybdenum diselenide as a saturable absorber. *Optical Eng.* **2016**, *55*. [CrossRef]
69. Du, J.; Wang, Q.K.; Jiang, G.B.; Xu, C.W.; Zhao, C.J.; Xiang, Y.J.; Chen, Y.; Wen, S.C.; Zhang, H. Ytterbium-doped fiber laser passively mode locked by few-layer Molybdenum Disulfide (MoS_2) saturable absorber functioned with evanescent field interaction. *Sci. Rep.* **2014**, *4*, 6346. [CrossRef] [PubMed]
70. Zhang, H.; Lu, S.B.; Zheng, J.; Du, J.; Wen, S.C.; Tang, D.Y.; Loh, K.P. Molybdenum disulfide (MoS_2) as a broadband saturable absorber for ultra-fast photonics. *Optics Express* **2014**, *22*, 7249–7260. [CrossRef] [PubMed]
71. Park, K.; Lee, J.; Lee, Y.T.; Choi, W.-K.; Lee, J.H.; Song, Y.-W. Black phosphorus saturable absorber for ultrafast mode-locked pulse laser via evanescent field interaction. *Ann. Phys.* **2015**, *527*, 770–776. [CrossRef]

72. Jhon, Y.I.; Koo, J.; Anasori, B.; Seo, M.; Lee, J.H.; Gogotsi, Y.; Jhon, Y.M. Metallic MXene saturable absorber for femtosecond mode-locked lasers. *Adv. Mater.* **2017**, *29*. [CrossRef]
73. Aiub, E.J.; Steinberg, D.; Thoroh de Souza, E.A.; Saito, L.A.M. 200-fs mode-locked Erbium-doped fiber laser by using mechanically exfoliated MoS_2 saturable absorber onto D-shaped optical fiber. *Optics Express* **2017**, *25*, 10546–10552. [CrossRef]
74. Khazaeinezhad, R.; Kassani, S.H.; Jeong, H.; Nazari, T.; Yeom, D.-I.; Oh, K. Mode-locked all-fiber lasers at both anomalous and normal dispersion regimes based on spin-coated MoS_2 nano-Sheets on a side-polished fiber. *IEEE Photonics J.* **2015**, *7*, 1–9. [CrossRef]
75. Long, H.; Liu, S.X.; Wen, Q.; Yuan, H.Y.; Tang, C.Y.; Qu, J.L.; Ma, S.N.; Qarony, W.; Zeng, L.H.; Tsang, Y.H. In_2Se_3 nanosheets with broadband saturable absorption used for near-infrared femtosecond laser mode locking. *Nanotechnology* **2019**, *30*, 465704. [CrossRef] [PubMed]

Disclaimer/Publisher's Note: The statements, opinions and data contained in all publications are solely those of the individual author(s) and contributor(s) and not of MDPI and/or the editor(s). MDPI and/or the editor(s) disclaim responsibility for any injury to people or property resulting from any ideas, methods, instructions or products referred to in the content.